Draft version June 8, 2021
Typeset using LaTeX **twocolumn** style in AASTeX61

COVARIANCE-REGULARIZED RECONSTRUCTION OF IMAGES

Michael R. Blanton[1]

[1] *Center for Cosmology and Particle Physics, Department of Physics, New York University, 4 Washington Place, New York, NY 10003, USA*

ABSTRACT

We discuss the problem of reconstructing an image from samples of its values, and show how a method called covariance regularized reconstruction (CRR) fits into a broader set of techniques addressing this problem. Specifically, we address the estimation of values on a rectangularly sampled grid based on a original set of irregular samples, and we focus on astronomical applications. This problem has a close mathematical relationship with deconvolution, image combination, sinc-shifting, other interpolation tasks, as well as gravitational lens reconstruction. We explain CRR, which we recently applied in the context of image reconstruction but which is based on similar techniques used in other contexts. We describe the relationship of CRR to other methods. Its major advantages are that, to the greatest extent possible, it retains the "native" spatial resolution of the original sampling while yielding images whose pixel values have uncorrelated errors. We describe the trade-offs between these advantages and the advantages of more traditionally-regularized deconvolution techniques. Finally, we show that for original samplings that are already rectilinear, the CRR technique is identical to techniques for shifting and combining samples already known under certain conditions to conserve the information in the images (for example, the sinc-shifting technique).

Corresponding author: Michael R. Blanton
michael.blanton@gmail.com

1. INTRODUCTION

This paper concerns the reconstruction of spatial or angular images with uniform sampling, based on experimental data with nonuniform, noisy sampling of varying spatial or angular resolution. Reconstructions of this nature are often desirable either for convenience or to consistently combine multiple data sets with different samplings. Here we concentrate on two-dimensional images and astronomical applications, but the techniques described herein are likely applicable in a broad range of circumstances.

We describe a method recently applied in this context called covariance-regularized reconstruction, that provides reconstructions whose individual pixel errors have low correlations with each other, which can be shown in certain circumstances to contain the same information content as the original samplings, and which appear to degrade the intrinsic resolution of the sampling very little. The goal of this paper is to compare this technique to other common methods and describe the interrelationships of these methods.

Imagine that there is some function defining an image. This function can be in any number of dimensions, but we will use the two-dimensional case for the examples here. Now imagine that the data you have about this image is some sampling of its values at certain locations. However this sampling has several properties, that are common in situations involving real data:

- The sampling isn't directly of the image, but of the image convolved with some resolution. So each sample is a projection of the image onto the "kernel" defining the resolution. The kernel may be different for each sample.
- The sampling is not on a rectilinear grid, and in fact may be of an arbitrarily irregular set of points.
- The sampling is noisy, in the sense that the values you get from the sampling are the resolution-convolved image samples, plus some random noise term. We will assume that the noise is independent in each sample and that it is Gaussian.

This basic description applies to a number of different astronomical data sets of interest. For example, shifting or rotating a normal image from a charge-coupled device (CCD) can be described in this fashion (though it doesn't necessarily need to be), as can the combination ("stacking") of multiple CCD images at different offset positions or with significant astrometric distortions. Integral field spectroscopy often produces image samples at each wavelength which are not on a rectilinear grid, and which due to chromatic atmospheric differential refraction are different for different wavelengths. Gravitational lenses are a perhaps surprising example, but the effect of the lens is only to change the kernel and the location of the sampling; thus, our description also applies to reconstructing source images behind gravitational lenses using a given mass model (for example, see **??**).

We should define the properties we would like our reconstruction to have in an ideal case:

- It should be on a rectilinear grid.
- It should minimally degrade the native resolution.
- Fitting models to the reconstruction using the errors should be equivalent to fitting the original set of samples.
- Errors in one pixel should have zero cross-correlation with errors in other pixels.

Importantly, our ideal case does not involve deconvolving the native resolution and emphasizes retaining the simple statistical properties for the errors (i.e. a diagonal covariance matrix). This emphasis is related to the fact that many of the applications we have considered can be low in signal-to-noise ratio; other definitions of ideal-ness might be appropriate in other situations. This description (in particular the last listed condition above) is equivalent to what **?** refer to as a "proper" image, and as we show in the Appendix B, their method is equivalent to the CRR method described here.

Section 2 describes a model problem, of irregular (also called scattered) data samples with heterogeneous kernels. Section 3 describes several classic approaches to this model problem. Section **??** describes and tests our method. Section **??** tests all the methods on the model problem against several benchmarks. Section **??** describes an application to IFU data. Section **??** describes an application to gravitational lens source modeling. Section **??** describes an application to shifting or rotating images and compares the method to classic sinc-kernel shifting. Section **??** describes an application to coaddition of images and compares the method and results to other methods.

2. MODEL PROBLEM

The *anzatz* we adopt is that there exists some image we would like to measure $R(x, y)$ where x and y represent some spatial or angular coordinates (here taken to be in a two-dimensional space, though the generalization to any other number of dimensions is straightforward). We have experimentally sampled this image in various locations which are arbitrarily well-known, the set of which can be expressed as a vector of values $\vec{x}$ and $\vec{y}$, or $\{x_j\}$ and $\{y_j\}$. Each sample has some intrinsic spatial resolution we refer to as a kernel $K_j(x, y)$; because of the experimental setup, each sample j is of the function $R(x, y) \otimes K_j(x, y)$. The sampling produces a set of fluxes $\vec{f}$, or $\{f_j\}$. The sampling is noisy with some standard deviation σ_j for each sample; each sample is statistically independent from the others. Using this nonuniformly

sampled data set $\vec{f}$ we want to infer a set of flux values $\vec{S}$ (or $\{S_i\}$) at a uniform rectilinear grid of pixel locations, which we will here refer to as a reconstruction.

Astronomical data can have all of these properties, found separately or together. First, a diffraction-limited telescope image has some a resolution that sets the minimal kernel width, and in many applications the atmosphere or the instrument provides an even broader kernel. When combining multiple images, the kernel can vary due to variations in the atmosphere or other effects. Some instruments, like the Gaia satellite, have gross asymmetries in their kernel, and the asymmetries are aligned differently with respect to the images for different samples. Gravitational lenses can create very heterogeneous kernels. Second, not all instruments have a rectilinear sampling (particularly integral field spectroscopy), and even when they do, multiple observations with the same instrument do not necessarily align. Gravitational lenses also effectively provide an irregular sampling of the source plane. Third, all of these observations have intrinsic noise, and we want to be able to reliably interpret them even in the noisy regime.

We will here define a specific model problem, where there are M samples distributed between $-10 < x < 10$ and $-10 < y < 10$. Each sample has a kernel which is symmetric Gaussian with a standard deviation chosen randomly, from a range we will choose differently in different cases but which will generally be ≥ 1. We will vary the noise from case-to-case as well. Figure 1 shows an example data set of this variety.

The problem we want to solve is to produce a two-dimensional grid of pixel values $\vec{S}$ that best represents (in the senses defined in the introduction) the underlying image $R(x, y)$. We will use a grid spacing of unity in our distance units, which will assure that our pixel grid always at least Nyquist samples all kernel-convolved images. We will place a central grid point at $(x, y) = (0, 0)$, and use $n_x = n_y = 21$, so the total number of grid points is $N = n_x n_y = 441$.

Before we begin, we make an observation about this model problem. Imagine we have an explicit model $\vec{m}$ for the observations whose parameters we desire to constrain. In that case, because the noise is Gaussian, the likelihood for the model parameters is $\mathcal{L} \propto \exp(-\chi^2/2)$, where

$$\chi^2 = \left(\vec{m} - \vec{f}\right) \cdot \mathbf{N}^{-1} \cdot \left(\vec{m} - \vec{f}\right), \tag{1}$$

and $\mathbf{N}$ is the covariance matrix of the samples, which we in this case is diagonal. If we manipulate the samples $\vec{f}$ in some way—say, by resampling them onto a uniform grid—and fit the model to the resampled data, we might in general change how χ^2 depends on the model parameters. However, if our resampling does not change how χ^2 depends on the model parameters, then it has retained effectively the same information as the original set of samples.

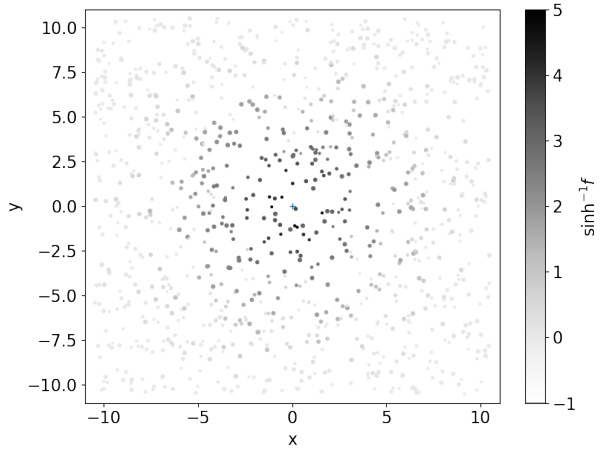

Figure 1. Example of data in the model problem, for $M = 1000$, with Gaussian standard deviations chosen randomly and uniformly between 1 and 4, and zero noise. Each point is a sample f_j, with a kernel width proportional to the point size, and the logarithm of the flux in the sample indicated by the color. The raw image is a point source at the center.

3. EXISTING APPROACHES TO THE PROBLEM

A number of methods exist to approach problems similar to that described above. We will discuss these here in order to put the motivation for our approach into context and to compare the performance of our method with existing methods.

We divide the methods into two general categories. The first category includes deconvolution methods, by which we mean here methods that seek to infer the original image $R(x, y)$. We introduce these methods because they help motivate our covariance-regularized reconstruction method, but also to point out important features of deconvolutions that affect whether we would choose to use them. We do not attempt a complete review of deconvolution methods.

The second category we broadly term reconstruction methods. These methods are harder to define in terms of their goals, but for a uniform kernel K most of them could be described as methods that seek to infer $R(x, y) \otimes K(x, y)$. Covariance-regularized reconstruction falls into this category.

3.1. *Deconvolution methods*

We introduce here some standard deconvolution methods. The goal of a deconvolution method is to infer the "undegraded" image $R(x, y)$ based on the samples of $R(x, y) \otimes K_j(x, y)$. Typically, we seek the values of $R(x, y)$ on a rectilinear grid in the x–y plane. If this deconvolution can be performed successfully there are obvious advantages to it. However, there are disadvantages as well that tend to be important in the presence of noise. First, in the presence of noise it is always nec-

essary to regularize the deconvolution, and that regularization involves arbitrary choices that render the estimate of $R(x,y)$ non-unique in ways that are hard to characterize. Second, the different values of $R(x,y)$ on the grid will inevitably have highly correlated errors, generally because neighboring pixels can usually trade signal between each other while still fitting the constraining data. Therefore, if noise is significant relative to the signal, then fitting the deconvolution to models requires tracking this covariance matrix. Standard regularization methods do not mitigate this effect, and can worsen it.

3.1.1. *Unregularized and Tikhonov-regularized models*

A straightforward way of approaching the model problem is to create a nonparametric image designed explicitly to explain our sampled fluxes. The idea is to determine a grid of pixel values $\vec{S}_F$, representing the amplitudes of a set of delta functions, that explain the sample values $\vec{f}$.

Since each sample j is the result of the convolution of the image $R(x,y)$ with a kernel $K_j(x,y)$, the expectation value $\vec{m}$ for the flux samples of a model consisting of pixel values $\vec{S}_F$ can be written as a linear transformation:

$$\vec{m} = \mathbf{A} \cdot \vec{S}_F. \tag{2}$$

Each column of $\mathbf{A}$ corresponds to a pixel in the nonparametric image, and each row of $\mathbf{A}$ corresponds to an observed sample; correspondingly, the values of the matrix are $A_{ji} = K_j(x_i, y_i)$. This model can perfectly reproduce any noise-free set of observations $\vec{f}$ so long as the narrowest kernel $K_j(x,y)$ is band-limited and is Nyquist sampled by the grid spacing; this claim arises from the derivation of the Nyquist limit for band-limited data. To fit the parameters in the model image $\vec{S}_F$ we minimize Equation 1 with this choice of $\vec{m}$.

Since $\vec{m}$ is linear in the model parameters ($\vec{S}_F$), this minization is quadratic and can be solved rapidly with matrix inversion to find the values of $\vec{S}_F$ that minimize χ^2. For example, they can solved through the normal equations:

$$\vec{S}_F = \left(\mathbf{A}^T \cdot \mathbf{N}^{-1} \cdot \mathbf{A}\right)^{-1} \cdot \mathbf{A}^T \cdot \mathbf{N}^{-1} \cdot \vec{f} \tag{3}$$

The covariance matrix $\mathbf{N}$ of the flux values $\vec{f}$ is diagonal in the cases we consider in this paper. The covariance matrix of $\vec{S}_F$ is given by:

$$\mathbf{C} = \left(\mathbf{A}^T \cdot \mathbf{N}^{-1} \cdot \mathbf{A}\right)^{-1} \tag{4}$$

We prefer here to use singular value decomposition (SVD) as follows:

$$\mathbf{N}^{1/2}\mathbf{A} = \mathbf{U} \cdot \Sigma \cdot \mathbf{V}^T \tag{5}$$

This decomposition is possible to achieve for any real matrices $\mathbf{A}$ and $\mathbf{N}^{1/2}$ in terms of real $\mathbf{U}$, $\mathbf{\Sigma}$, and $\mathbf{V}$, where $\mathbf{\Sigma}$ is diagonal, $\mathbf{V}$ is orthogonal ($\mathbf{V}\mathbf{V}^{\mathrm{T}} = \mathbf{1}$), and $\mathbf{U}$ is close to orthogonal ($\mathbf{U}\mathbf{U}^{\mathrm{T}}$ is diagonal with ones for dimensions i with $\Sigma_i \neq 0$ or zeros for dimensions i with $\Sigma_i = 0$).

That makes the inversion of the problem easy so it is:

$$\begin{aligned}\vec{S}_F &= \mathbf{V} \cdot \Sigma^{-1} \cdot \mathbf{U}^T \cdot \mathbf{N}^{-1/2} \cdot \vec{f} \\ &= \mathbf{W}_F \cdot \vec{f}\end{aligned} \tag{6}$$

In general, some values along the diagonal of Σ may be zero or very small (e.g. at double precision, of order 10^{-15} or so the maximum value in Σ). When this occurs, the covariance matrix is nearly or completely degenerate (non-invertible). In the inversion above, we use the standard Moore-Penrose pseudo-inverse technique and take $\Sigma_{ii}^{-1} = 0$ if $\Sigma_{ii} = 0$ (or very small). In non-degenerate cases (when there is not a large dynamic range in Σ) the result is identical to that found using the normal equations; in degenerate cases, an infinite number of solutions exist and the pseudo-inverse returns the solution that minimizes the norm $|\vec{S}_F|^2$.

The upper left panel of Figure 2 shows the results of this method in the case there is no noise in the image. It works essentially perfectly, as it should. This result shows how this method works like a deconvolution—the kernel is fully deconvolved out of the image model.

Under even a small amount of noise, however, this method is very unstable. The upper middle panel of Figure 2 shows the results of adding noise per pixel at a level of 10^{-3} of the total flux. A considerable amount of unnecessary noise is added; in fact these effects appear even for much smaller amounts of noise.

We can understand the source of this effect by looking at the covariance matrix of the results. The covariance matrix can be written:

$$\begin{aligned}\mathbf{C}_F &= \mathbf{W}_F \cdot \mathbf{N} \cdot \mathbf{W}_F^T \\ &= \left(\mathbf{V} \cdot \mathbf{\Sigma} \cdot \mathbf{\Sigma} \cdot \mathbf{V}^T\right)^{-1}\end{aligned} \tag{7}$$

It is useful to look at the correlation matrix, which is defined as:

$$\frac{C_{F,ij}}{\sqrt{C_{F,ii}C_{F,jj}}}. \tag{8}$$

The upper right panel of Figure 2 shows a section of this correlation matrix. Clearly there are many strong correlations among pixels. It is clear that what is happening is that neighboring pixels can generally cancel each other out in their contribution to each sample, so they can become arbitrarily large in the negative or positive direction, as long as their neighbors take the opposite sign and cancel them out. This problem could be reduced by taking larger pixels, but a much coarser grid would not sample the kernel resolution well, which would reduce its ability to take best advantage of the data.

A common method to control this sort of degeneracy is through a regularization method. The simplest

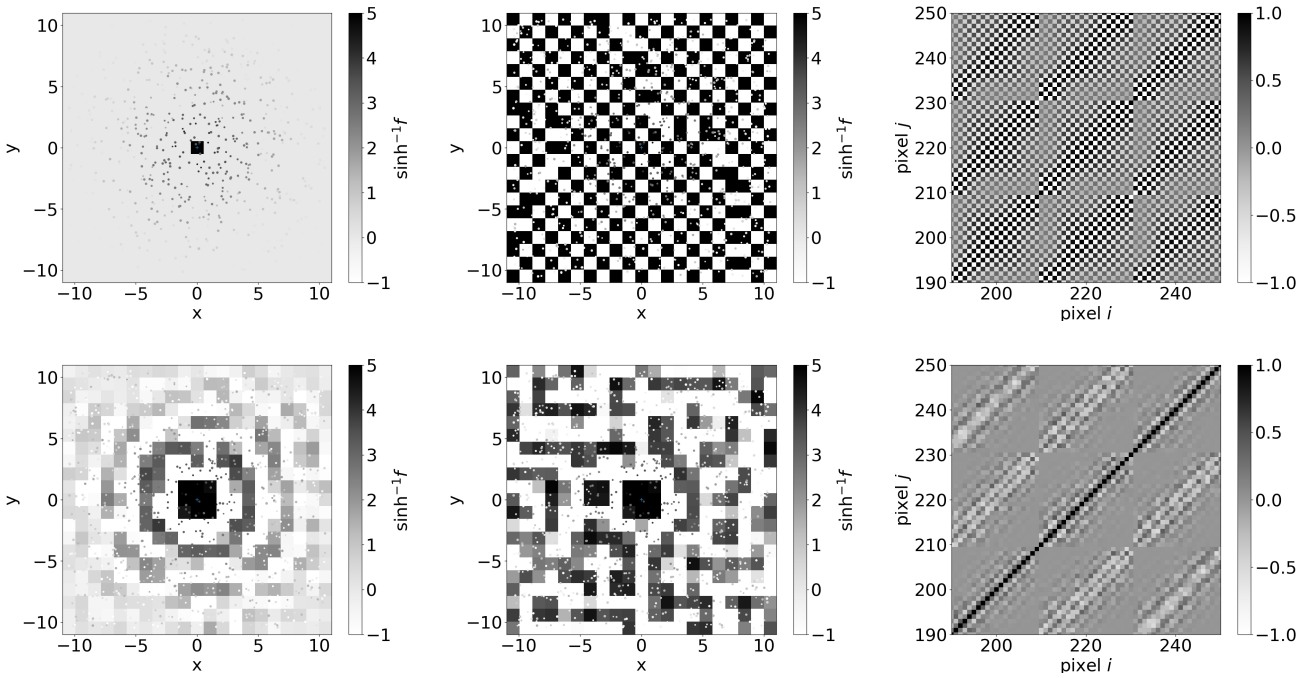

Figure 2. Image reconstructions and correlation matrices using the methods of Section 3.1.1. For each image reconstruction (left and middle columns), the dots show the function sampling locations and values, and the background image shows the reconstruction. Each panel uses the same set of sample locations and kernels, for a point source at the image center. The left column can be thought of as the PSF of the observations combined with the reconstruction method. For each method, we show a small section of the correlation matrix $C_{ij}/\sqrt{C_{ii}C_{jj}}$ near the diagonal (right columns). *Upper left:* Unregularized linear model applied to noiseless data. *Upper middle:* Unregularized linear model applied to data with noise per sample 10^{-3} of the total flux. *Upper right:* Correlation matrix for unregularized linear model fit, showing large off-diagonal terms. *Lower left:* Tikhonov-regularized linear model applied to noiseless data, with $\lambda = 10^{-2}$. *Lower middle:* Tikhonov-regularized linear model applied to noisy data, with $\lambda = 10^{-2}$ and noise per sample 10^{-3} of the total flux. *Lower right:* Correlation matrix for Tikhonov-regularized linear model.

such method is Tikhonov regularization, which modifies Equation 1 with the addition of a term quadratic in the model parameters:

$$\chi^2 = \left(\vec{m} - \vec{f}\right) \cdot \mathbf{N}^{-1} \cdot \left(\vec{m} - \vec{f}\right) + \lambda^2 \left|\Gamma \cdot \vec{S}_T\right|^2 \quad (9)$$

where in this case $\vec{m} = \mathbf{A} \cdot \vec{S}_T$ and $\vec{S}_T$ represents the Tikhonov-regularized result for some choice of Γ and λ. An example of this usage can be found in **?**. If Γ is the identity matrix, this problem can be reduced to a simple substitution of Σ_{ii}^{-1} with $\Sigma_{ii}/(\Sigma_{ii}^2 + \lambda^2)$ in Equation 6.

More complicated choices of Γ lead to problems that are still linear but that standard SVD does not conveniently decompose. However, a generalized SVD (GSVD) exists that does so. For the two matrices $\mathbf{N}^{-1/2} \cdot \mathbf{A}$ $(M \times N)$ and $\mathbf{\Gamma}$ $(N \times N)$, a special case of GSVD is the decomposition:

$$\begin{aligned} \mathbf{N}^{-1/2} \cdot \mathbf{A} &= \mathbf{U} \cdot \Sigma_1 \cdot \mathbf{R} \cdot \mathbf{Q}^T \text{ and} \\ \mathbf{\Gamma} &= \mathbf{V} \cdot \Sigma_2 \cdot \mathbf{R} \cdot \mathbf{Q}^T, \end{aligned} \quad (10)$$

where $\mathbf{Q}$ is $N \times N$ and orthogonal, $\mathbf{U}$ is $M \times M$ and orthogonal, $\mathbf{R}$ is $N \times N$ and non-singular, $\mathbf{V}$ is $N \times N$ and orthogonal, Σ_1 is $M \times N$ and diagonal, and Σ_2 is $N \times N$ and diagonal. With this decomposition the solution becomes:

$$\vec{S}_T = \mathbf{Q} \cdot \mathbf{R}^{-1} \cdot \left(\Sigma_1^T \cdot \Sigma_1 + \lambda^2 \Sigma_2^2\right)^{-1} \cdot \Sigma_1^T \cdot \mathbf{U}^T \cdot \vec{f} \quad (11)$$

This approach is preferable to simply solving the normal equations for Equation 9 because it requires only one non-trivial inverse for many different choices of λ and because it allows the identification of the modes of the solution that are affected by the regularization.

A simple but nontrivial choice for Γ is designed to reduce the differences between each pixel value and the average of its neighbors. For this choice, each row of Γ has 1 in the diagonal element and $-1/4$ in each element correponding to one of the four closest pixels. The rows of Γ corresponding to edge and corner pixels instead have off-diagonal values of $-1/3$ and $-1/2$ respectively.

The bottom left panel of Figure 2 shows the results of using this regularization under our model problem, with $\lambda = 10^{-2}$ and no noise in the data. This image can be thought of as the PSF resulting from the combination of the image sampling and the reconstruction technique.

This resulting PSF is narrow, but has interesting ringing features whose origin is not obvious. Features similar to these also occur for $\Gamma = \mathbf{I}$. These features become more pronounced, and different choices of Γ yield more dissimilar results, as λ becomes larger.

The bottom middle panel of Figure 2 reveal the advantage of regularization when noise is added with an amplitude per sample of 10^{-3} of the total flux. Unlike the unregularized case, the general features of the noiseless image are maintained, including the ringing features of the PSF. With our parameter choices in this example, these ringing features are mostly subsumed into the noise.

As the bottom right panel of Figure 2 shows, the noise itself exhibits correlations from pixel to pixel. These correlations vary significantly depending on the exact relationship between the sample locations, the sample kernels, and the pixel locations, and can be both negative and positive. In our example, the correlation coeffients are 0.15–0.20 out to separations of about three pixels, and slowly decline after that; the typical pixel has ~ 40 near neighbors with a correlation coefficient greater than 0.15. So in this example, fitting a model to the deconvolved data is highly affected by these correlations if they are not properly accounted for. Any time deconvolution is performed the impact of the non-trivial correlation matrix needs to be evaluated to determine if it is important to the problem at hand (which it may not always be).

In the Tikhonov regularization, λ is a free parameter, as is the detailed form of Γ. Even very small λ tends to reduce the worst "checkerboard" features of the correlation matrix, but neighboring pixels remain highly anticorrelated. As λ is increased neighboring pixels transition from anticorrelated to correlated and a broad positive correlation developed near the diagonal of the correlation matrix. Meanwhile, as λ increases the PSF becomes broader and broader. The exact nature of the dependence on regularization depends on a combination of the kernel size and the reconstruction pixel scale, and must be carefully evaluated for any deconvolution.

A key aspect of Figure 2 is to recognize that the PSF and the correlation matrix probe two different features of a regularized deconvolution or any other sort of reconstruction. Qualitatively, the PSF probes the coupling of the signal in neighboring pixels, whereas the correlation matrix probes the coupling of the noise in neighboring pixels. They both must be known to characterize the relationship between a model for the underlying image and the result obtained by the combination of our instrument and our analysis.

3.1.2. *Linear models with nonnegative constraints*

The linear deconvolution method can be adjusted by adding regularization conditions that are not linear (i.e. are more complex than the Tikhonov varity of methods). Nonnegative constraints are tempting because we often expect the signal to be nonnegative, and yet the degeneracies above arise in part from the fact that the solutions' pixel values are allowed to be negative as well as positive.

Nonnegatively constrained deconvolution involves minimizing Equation 1 under the conditions that $\vec{S}_F \geq 0$. Standard techniques in quadratic programming exist that can readily solve the linear problem under these constraints, at least at the scale of our toy problem. In the case of zero noise, the results are exactly the same as the linear deconvolution method. That is, the method successfully reconstructs a delta function source at the center.

The effect of the nonnegative constraint becomes apparent in the presence of noise. Figure 3 shows the results for a point source at the center with noise per sample of 10^{-3} of the total flux. The left panel shows a single realization. This result shows the power of the constraint; an extremely sharp image is recovered without degeneracies appearing.

We can ask further what the mean response is to a point source, by running 24,000 realizations. The middle left and middle right panels show this mean response for two noise levels. The mean response is not as narrow as each individual response, and the mean response appears to depend on the signal-to-noise ratio. The far right panel shows the radial profile of the mean response for three different noise levels (passing through the location of the point source).

Two effects appear in Figure 3. First, a background is evident, that becomes larger at higher noise levels. This background is due to the fact that noise fluctuations above zero lead to a response in the image but noise fluctuations below zero lead to zero response. For Gaussian noise and a zero true signal, the level of bias can be shown to be on average $\sigma/\sqrt{2\pi N_{\rm eff}}$, where $N_{\rm eff}$ is the effective number of samples contributing to each pixel. It must be that $N_{\rm eff} \propto \rho\sigma_g^2$, with ρ being the density of samples per pixel; for a constant σ_g the constant of proportionality is 4. The horizontal lines in Figure 3 show this bias level estimated for the simulation. For a non-zero true signal, the level of bias will be less, but the bias is not possible to predict *a priori* because the true signal is not known, which complicates statistical analysis of the resulting image.

Second, the response becomes broader at higher noise levels, so that the response is signal-to-noise ratio dependent. This nonlinearity is a symptom of the nonlinearity of the method and a demonstration of the fact that the mean response is not the PSF of the method. For linear methods the mean of the realizations would be the same as the noiseless solution, because the linear operations of the method commute with the mean. For nonlinear methods this commutation no longer holds. Thus, there is no PSF, or in mathematical terms no Green's function, that generally characterizes the response.

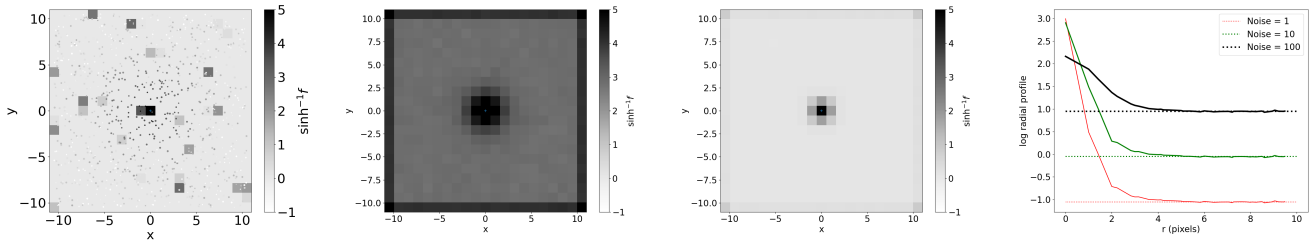

Figure 3. Results for nonnegative least squares method applied to a point source input. *Left:* Single realization with noise per sample of 10^{-3} of the total flux. *Middle left:* Mean of 1000 realizations with noise per sample of 0.1 of the total flux. *Middle right:* Mean of 1000 realization with noise per sample of 10^{-3} of the total flux. *Right* Slice through mean of 25,000 realizations, for three noise levels (relative to a total flux of 1000), as labeled.

Figure 4. Results for nonnegative least squares method applied to a uniform signal distribution. *Left:* Single realization with noise per sample of 10^{-2} of the total flux. *Middle left:* Subsection of the covariance matrix based on 1000 Monte Carlo realizations. *Middle right:* Distribution of pixel values. *Right:* Joint distribution of pixel values of neighboring pixels; each point is a pair of pixels. For clarity near zero we have added a small amount of extra noise.

Another interesting case is the case of a uniform background within the image area. This case characterizes how these deconvolutions will work for more diffuse or extended sources. Unlike for linear methods, the results for extended sources are not just a sum of the PSF response, so we need to characterize them separately. The left panel of Figure 4 shows the result of fitting the results in the presence of noise per sample at about 1% of the background signal. For a diffuse background, the nonnegative constraints still allow large fluctuations around that mean diffuse value.

We can study these fluctuations with the covariance matrix, though as we show below in this case the covariance matrix does not sufficiently characterize the statistics of the noise. In this case, we need to use a set of Monte Carlo realizations to determine the covariance matrix. The middle left panel of Figure 4 shows a section near the diagonal of this covariance matrix estimated from a 1000 realizations. There are strong negative off-diagonal values in this covariance matrix, indicative of the degeneracies described above.

The covariance matrix completely describes the distribution of a multivariate Gaussian about its mean. However, the fluctuations in the nonlinear case are far from Gaussian even when the input errors are Gaussian. The middle right panel and right panels of Figure 4 demonstrate this non-Gaussianity, with the probability distribution of pixel values and with the joint distribution of these probabilities. There is a clear anticorrelation of values when they are both non-zero, but in most cases one or the other pixel of the pair is zero. A distribution like this one is not fully characterized by a Gaussian and an analysis of this image that accounted for the errors would not be correct if it assumed a Gaussian distribution of errors.

The consequences of these properties are that characterizing the resolution and noise of a nonlinear deconvolution, even the simplest variety, can be complex. Typically, we do expect however that these issues become less significant at higher signal-to-noise ratio.

We remark here briefly on the relationship between this method and Richardson-Lucy deconvolution, which is commonly used in astronomy. Richardson-Lucy maximizes the likelihood under a Poisson model for the measured samples. The Poisson model is naturally nonnegative. Like linear model with nonnegative constraints, it is a nonlinear method and has very similar pitfalls. If the noise in the image is background Poisson noise dominated (and the background is subtracted, not part of the deconvolution), in fact Richard-Lucy decomposition reduces to the nonnegative least squares technique. Specifically, while its performance can be reasonable for point sources, for extended distributions it suffers from degeneracies that need to be regularized. The Richardson-Lucy method is iterative, and a common regularization is to provide a stopping condition before convergence; this regularization is meant to avoid exploration of the degeneracies associated with diffuse light. The stopping condition requires an adjustable parameters, and of course its efficacy must depend on the initial conditions of the iteration as well. We do not explore this method further here.

3.1.3. *Maximum Entropy Reconstruction*

The third variant of deconvolution we discuss is maximum entropy. Like Tikhonov regularization, this method minimizes the χ^2 found in Equation 1 plus a regularization term. In this case, the regularization term is related to the information entropy of the reconstruction:

$$\chi^2_{\rm MEM} = \chi^2 + \lambda \sum_i S_{{\rm MEM},i} \ln S_{{\rm MEM},i}, \qquad (12)$$

where λ is a tunable regularization parameter. Though it is not a linear problem, this objective can be readily

minimized with standard minimization techniques for the scale of problem we consider here.

Figure 5 shows the result of this method for our standard point source, using $\lambda = 10^{-2}$. These results do not depend strongly on this regularization parameter. Each panel is the same as in Figure 3. The results are remarkably similar, showing the same biases as the signal-to-noise ratio decreases. These biases therefore appear to derive in large part from the nonnegative nature of the maximum entropy method.

Figure 6 shows the result of this method for a uniform illumination, using $\lambda = 10^{-2}$. In this case, the regularization parameter matters—a much smaller λ leads to a result more similar to that found in Figure 4. The resulting correlation matrix, however, has many of the same features for maximum entropy—it is still the case that there are anticorrelations between neighboring pixels. In addition, the error distribution is also non-Gaussian, though considerably less so than for nonnegative fitting.

3.1.4. *Summary*

There are many more techniques of deconvolution, tuned to and appropriate for numerous circumstances. The very short tour above is meant only to introduce some of the basic features of deconvolution in the context here. The crucial features are as follows. First, deconvolution can produce extremely sharp images. As the signal-to-noise ratio increases, a reasonably regularized deconvolution can produce a very sharp image. Second, the PSF of the deconvolution tends to be either unusual (in the case of regularized linear deconvolution) or nonexistent, with a response that is signal-to-noise ratio dependent (in the case of nonlinear methods). Third, many deconvolution methods require a tunable parameter whose appropriate value depends on the data of the image being reconstructed. Fourth, the errors in deconvolutions tend to be poorly behaved; in all cases above, they either have strong off-diagonal covariances or strong non-Gaussianities. The last three features mean that there is no uniquely defined, generally applicable procedure for deconvolution; all applications of deconvolution in the presence of finite noise require the investigator to evaluate trade-offs in the regularization procedure to determine what behavior is tolerable in their application.

The point of this discussion is not to criticize any particular application of deconvolution. Many valid and useful applications of deconvolution exist; indeed, in many cases the problems identified in this subsection are minor or negligible. This discussion is meant to provide background, context, and motivation for the covariance-regularized reconstruction described later.

3.2. *Interpolation methods*

Interpolation methods have perhaps less ambitious goals than deconvolution methods. They do not seek to remove the effect of the instrumental resolution, but seek instead to estimate the image in between the samples. For a uniform kernel K, they might be approximately described as methods that seek to infer $R(x,y) \otimes K(x,y)$, whereas deconvolution methods seek to infer $R(x,y)$. We will review here several reconstruction methods

3.2.1. *Shepard's method*

The method of **?** or its variants are the most commonly used for problems like our model problem; for example **?** and **?** use the method in the context of integral field spectroscopy in astronomy. Many variants of this method with different weighting function have been studied in the literature, though they all share the essential features our simple weight function has, namely that they are smooth, all positive, stationary functions (**?**).

The basic idea is to transform the measured fluxes at each sample to a value at each grid point using a set of linear weights:

$$\vec{S}_S = \mathbf{W} \cdot \vec{f} \tag{13}$$

where the weights W_{ij} are set using some stationary function of the distance r_{ij} between the grid point i and the sample j.

A simple weight function is a circularly symmetric Gaussian with standard deviation σ_0:

$$W_{ij} = \frac{1}{W_{0,i}} \exp\left(-\frac{r_{ij}^2}{2\sigma_0^2}\right), \tag{14}$$

for $r_{ij} < r_{\rm lim}$, and zero otherwise. $W_{0,i}$ is defined as the sum of the N weights for each output grid point i, to guarantee the conservation of flux:

$$W_{0,i} = \sum_j \exp\left(-\frac{r_{ij}^2}{2\sigma_0^2}\right), \tag{15}$$

over all pixels i for which $r_{ij} < r_{\rm lim}$.

For the model problem, Figure 7 shows the result of Shepard's method for $\sigma_0 = 1$, given a point source input. Since this method is purely linear, the image can be thought of as the Point Source Function (PSF) of the experiment and method combination.

Obviously the PSF for Shepard's method is much broader than for the deconvolution methods, by construction. It reflects both the resolution of the kernel and to some extent the choice of the weights W_{ij}. In our test case, the resolution of the kernel is variable, so its exact effect is unclear. Therefore, we tested the effect of Shepard's method on the resolution by testing a case with a constant kernel. We found that the best-fit Gaussian width $\sigma_{\rm PSF}$ of the PSF was well-approximated by the combination in quadrature of the kernel width σ and the σ_0 used by Shepard's method. We conclude that Shepard's method tends to degrade the image relative to the kernel-convolved image.

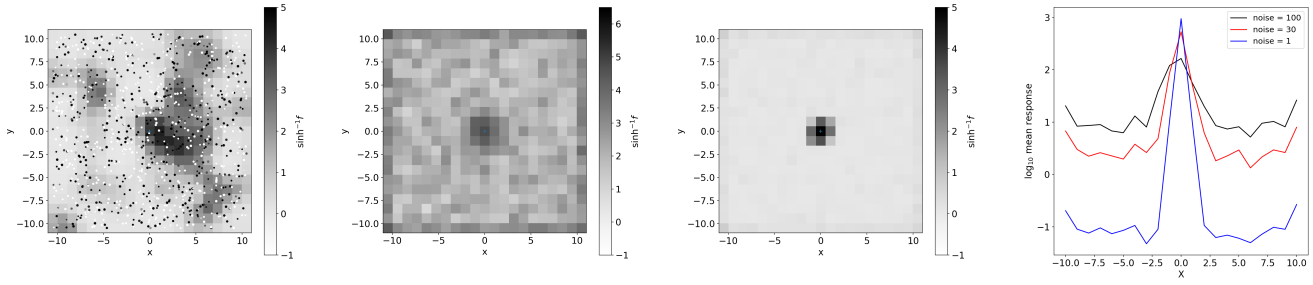

Figure 5. Similar to Figure 3, for the maximum entropy method applied to a point source input.

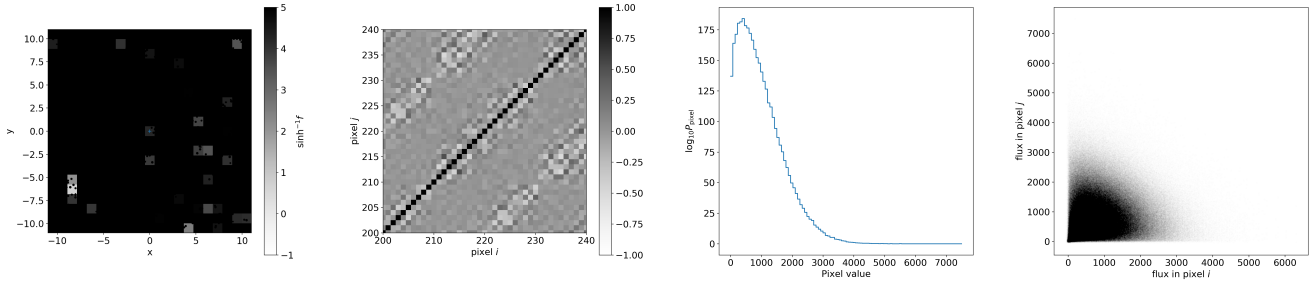

Figure 6. Similar to Figure 4 for the maximum entropy method applied to a uniform signal distribution.

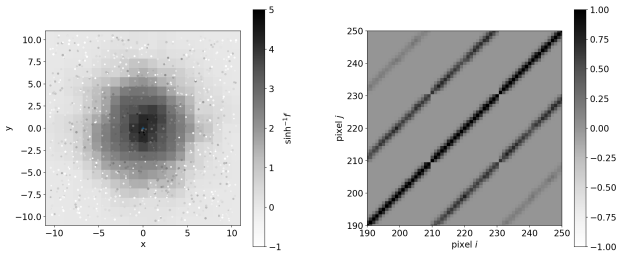

Figure 7. *Left panel*: Shepard's method for noiseless case. *Right panel*: Subsection of the covariance matrix of Shepard's method.

In addition, Shepard's method exhibits a broad non-diagonal correlation matrix. In this case, unlike the deconvolution, there are positive correlations between neighboring pixels instead of negative ones. This correlation is caused by the fact that errors in the samples will affect neighboring pixels in very similar ways; if a sample fluctuates upward or downward, a bunch of neighboring pixels fluctuate upward or downward together.

3.3. *Gaussian Process Regression*

4. COVARIANCE-REGULARIZED RECONSTRUCTION

In this paper, we present a different approach to reconstruction, whose goals and methods are informed by the previous methods discussed above. Like the model-fitting approaches discussed above, we seek a reconstructed image that is consistent with all of the input data. However, instead of regularizing the values of the fully-deconvolved images, the method reports a reconstructed image equal to the fully-deconvolved image, reconvolved with a point spread function designed so that each reported pixel value is statistically independent. That is, we desire that the covariance matrix of the pixel values is diagonal.

This goal has the following implications:

- The pixel values do not have the anticorrelations that are present in the full deconvolution. This fact leads to a smooth image that avoids the amplification of noise.

- The resulting image can be analyzed without accounting for off-diagonal covariances, which simplifies subsequent analysis.

Like some of the techniques above, it involves constructing a model that explains all of the data. However, instead of regularizing that model through smoothness, nonnegativity, or entropy criteria, we regularize the covariance between pixels in our outputs model. Specifically, we seek a method that guarantees zero off-diagonal covariance. The resulting image is related to the true deconvolved image through a known PSF; indeed, the result is very similar to performing a full deconvolution and then reconvolving with the native resolution.

We begin with the covariance of the fully deconvolved image $\vec{S}_F$:

$$\mathbf{C}_F = \mathbf{V} \cdot \mathbf{\Sigma}^{-2} \cdot \mathbf{V}^T \tag{16}$$

We seek to linearly transform $\vec{S}_F$ into a new quantity $\vec{S}_G$ with the property that its covariance matrix is diagonal if the input values $\vec{f}$ also have a diagonal covariance matrix.

It is straightforward to verify that the matrix $\mathbf{V}$ consists of the eigenvectors and $\mathbf{\Sigma}^{-2}$ of the eigenvalues of the covariance $\mathbf{C}_F$. The transformation $\mathbf{V}^T \cdot \vec{S}_F$ therefore will yield a vector whose covariance is diagonal. However, this new vector would redistribute the signal into a set of modes sorted by variance. Whereas each entry in $\vec{S}_F$ is associated with a pixel in the image, each entry in $\mathbf{V}^T \cdot \vec{S}_F$ would be some combination of pixels without any necessary geometric relationship with the pixel associated with the corresponding entry in $\vec{S}_F$.

Instead consider the following transformation:

$$\mathbf{R} = \mathbf{Q}_S \cdot \mathbf{Q} = \mathbf{Q_S} \cdot \mathbf{V} \cdot \mathbf{\Sigma} \cdot \mathbf{V}^T, \tag{17}$$

where $\mathbf{Q}_S$ is any diagonal matrix and $\mathbf{Q}$ can also be interpreted as the inverse of the square root of the covariance matrix:

$$\mathbf{C}_F = \mathbf{Q}^{-1} \cdot \mathbf{Q}^{-1}. \tag{18}$$

From right to left, the operator $\mathbf{R}$ in Equation 17 first uses $\mathbf{V}^T$ to rotate $\vec{S}_F$ into a space where the covariance is diagonal. Then it rescales each axis in this space by $\mathbf{\Sigma}$, which makes the covariance matrix the identity matrix. Then it uses $\mathbf{V}$ to rotate back to the original axes. This orients the vector such that its entries may be associated directly with the original pixels. Because the covariance has been "whitened," i.e. made spherically symmetric by multiplying by $\mathbf{\Sigma}$, prior to the rotation back, the covariance remains diagonal. Thus, the net transformation is to rescale the vector along the principal axes of the covariance matrix.

Because $\vec{S}_F$ is meant to represent an image, this rescaling can change properties of the result that we would like instead to remain unchanged; for example, we expect that our transformation should not add or subtract signal from the image, but the tranformation $\mathbf{V} \cdot \mathbf{\Sigma} \cdot \mathbf{V}^T$ will in general do so. Luckily, we may multiply by any diagonal matrix $\mathbf{Q}_S$ and the covariance remains diagonal. We thus define

$$Q_{S,ij} = \frac{\delta_{ij}}{\sum_{j'} Q_{ij'}}. \tag{19}$$

Then $\mathbf{Q}_S$ has the property that the flux in $\vec{S}_F$ is conserved.

We then see that:

$$\begin{aligned}\vec{S}_G &= \mathbf{W}_G \cdot \vec{f} \\ &= \mathbf{R} \cdot \mathbf{W}_F \cdot \vec{f} \\ &= \mathbf{Q_S} \cdot \mathbf{V} \cdot \mathbf{\Sigma} \cdot \mathbf{V}^T \cdot \mathbf{V} \cdot \mathbf{\Sigma}^{-1} \cdot \mathbf{U}^T \cdot \mathbf{N}^{-1/2} \cdot \vec{f} \\ &= \mathbf{Q_S} \cdot \mathbf{V} \cdot \mathbf{U}^T \cdot \mathbf{N}^{-1/2} \cdot \vec{f}\end{aligned} \tag{20}$$

and then we can show:

$$C_{G,ij} = Q^2_{S,ij} \delta_{ij}. \tag{21}$$

As we will show explicitly below, $\mathbf{R}$ represents the PSF of the resulting image; if the native PSF is constant among the samples, it is equal to that.

One issues arises with this method as described, which is that because $\mathbf{N}^{-1}$ enters the procedure, the PSF depends on the noise estimate. If the noise estimate depends on the signal itself (for example because the image is the result of a Poisson process) then the recovered PSF is a function of the signal, which in many applications is undesirable. Therefore, we recommend replacing $\mathbf{N}^{-1}$ with $\tilde{\mathbf{N}}^{-1}$, defined to be 1 if $\mathbf{N}^{-1}$ is greater than zero and 0 if $\mathbf{N}^{-1}$ is equal to zero.

This method has an interesting relationship with interpolation methods for regular grids. Nyquist-sampled images on rectangular grids (or images that are easily deformable to rectangular grids) can be perfectly interpolated using a sinc kernel. Under a pure shift (i.e. not under a rotation, scale, or other deformation), and for constant noise with a diagonal covariance, the shifted image also has a diagonal covariance matrix. Strictly, these properties hold only for images infinite in size. Note that usually sinc interpolation is modified in practice by damping the kernel at large radius. As we show in the Appendix, the covariance-regularized reconstruction method described above is identical to sinc interpolation for pure shifts in the limit of infinite size images of constant noise.

This method is also closely related to the construction of "proper" image coadds from individual images of varying PSF, as described by **?**. **NEED TO DO THE MATH AND SEE IF THIS IS TRUE**.

Although we relegate the lengthy proofs of these statements to the Appendix, in both cases the perhaps surprising result is ultimately a consequence of the properties of the SVD of circulant matrices. Specifically, the eigenvectors of such matrices are the discrete Fourier modes. This property yields an analytic result for the SVD and for the weights $\mathbf{W}_G$ under a shift. **BUT UNCLEAR WHERE IT COMES FROM FOR PROPER COADDS**.

5. SUMMARY

We thank people. David W. Hogg. Robert H. Lupton. Mike O'Neil. Adam S. Bolton. David J. Schlegel. David R. Law.

APPENDIX

A. SINC INTERPOLATION AND COVARIANCE-REGULARIZED RECONSTRUCTION

Sinc interpolation is interpolation from a uniform grid using the kernel:

$$\mathrm{sinc}\left(\frac{x}{\Delta}\right) = \frac{\sin\left(x/\Delta\right)}{x/\Delta} \tag{A1}$$

where Δ is the grid spacing. The two-dimensional version of sinc interpolation is simply the one-dimensional version applied separately in each dimension.

For infinitely large, perfectly Nyquist-sampled images, sinc interpolation is perfect—the original image samples fully specify the sampled function, and the sinc interpolation method perfectly reproduces it. Under the same conditions, plus the condition of constant noise with a diagonal covariance (that is, no noise correlation between pixels), then if you shift an image using sinc interpolation, the noise in the resulting image has the same noise as the original pixels and still has a diagonal covariance. This last property does not hold for rotations, rescalings, or other deformations of the image.

In practice, sinc interpolation is usually modified by damping the kernel at large scales. Doing so can limit the effects of artifacts due to the image not being Nyquist sample or having varying noise (most particularly, if extreme value parts of the image have larger noise, which can cause "ringing" in the result). However, in this Appendix we will compare covariance-regularized reconstruction to undamped sinc interpolation.

We first consider how we would use covariance-regularized reconstruction to shift an image in the case of a constant PSF. In this case the original image on a rectilinear grid is $\vec{f}$ and the fully deconvolved, shifted image inferred is $\vec{S}_F$. Taking for the moment the one-dimensional, periodic case, the matrix $\mathbf{A}$ would have the property that each row consists of the same $\vec{h}$, shifted by some integer number of columns. This type of matrix is called circulant. In two dimensions, this property does not hold any more because of the effects of the edges, and of course physical images are not typically periodic. Nevertheless, we are going to be considering the limit that the image becomes infinitely large, in which limit it can be considered arbitrarily close to circulant.

Each row $\vec{h}$ is the assumed PSF, with samples offets by the desired amount of the shift. In the calculation below we will assume that the image is band-limited, in which case we will see that the exact form of $\vec{h}$ does not change the result.

Circulant matrices have the property that their eigenvectors are the discrete Fourier modes. This fact can be used to calculate their SVD explicitly. As shown by Romberg (2011) [1] for an $n \times n$ matrix:

$$V_{mk} = \begin{cases} \frac{1}{\sqrt{n}} & k = 0 \\ \frac{2}{\sqrt{n}} \cos\left(2\pi km/n\right) & k = 1 \ldots \left(\frac{n}{2} - 1\right) \\ \frac{z_0}{\sqrt{n}} \left(-1\right)^m & k = \frac{n}{2} \\ \frac{2}{\sqrt{n}} \sin\left(2\pi km/n\right) & k = \left(\frac{n}{2} + 1\right) \ldots (n-1) \end{cases}, \tag{A2}$$

$$U_{mk} = \begin{cases} \frac{z_0}{\sqrt{n}} & k = 0 \\ \frac{2}{\sqrt{n}} \cos\left(2\pi km/n + \theta_k\right) & k = 1 \ldots \left(\frac{n}{2} - 1\right) \\ \frac{z_{n/2}}{\sqrt{n}} \left(-1\right)^m & k = \frac{n}{2} \\ \frac{2}{\sqrt{n}} \sin\left(2\pi km/n + \theta_k\right) & k = \left(\frac{n}{2} + 1\right) \ldots (n-1) \end{cases}, \text{ and} \tag{A3}$$

$$\Sigma_{mk} = \delta_{km} \left|\hat{h}_k\right|, \tag{A4}$$

where θ_k is the complex phase of $\hat{h}_k$ and $z_k = \mathrm{sgn}(\hat{h}_k)$. Note that to keep V_{mk} real the Fourier modes are here expanded in sin and cos instead of their complex exponential form.

In our case, because $\vec{h}$ is real, positive, and band-limited, $\hat{h}_0$ is real and equal to the sum of all the h_k, and $h_{n/2} = 0$, which further means that $z_0 = 1$ and $z_{n/2} = 0$. Furthermore, $\hat{h}_k = \hat{h}^*_{n-k}$. We will also take $\mathbf{N}^{-1/2} = 1$. From this expression of the SVD of a circulant matrix, we can then calculate $\mathbf{Q}_S \cdot \mathbf{V} \cdot \mathbf{U}^T$ directly.

[1] http://pwp.gatech.edu/wp-content/uploads/sites/436/2011/04/circsvd-notes.pdf

We start by calculating **Q**:

$$\begin{aligned} Q_{ml} &= \sum_{k=0}^{n-1} V_{mk}\Sigma_{kk}V_{lk} \\ &= \frac{\left|\hat{h}_0\right|}{n} + \sum_{k=1}^{n/2-1} \frac{2}{n}\cos\left(2\pi km/n\right)\cos\left(2\pi kl/n\right)\left|\hat{h}_k\right| \\ &\quad + \frac{\left|\hat{h}_{n/2}\right|}{n}\left(-1\right)^{m+l} + \sum_{k=n/2+1}^{n-1} \frac{2}{n}\sin\left(2\pi km/n\right)\sin\left(2\pi kl/n\right)\left|\hat{h}_k\right| \end{aligned} \tag{A5}$$

By replacing $k = n - k'$ in the second summation we find:

$$\begin{aligned} Q_{ml} &= \frac{\left|\hat{h}_0\right|}{n} + \sum_{k=1}^{n/2-1} \frac{2}{n}\cos\left(2\pi km/n\right)\cos\left(2\pi kl/n\right)\left|\hat{h}_k\right| \\ &\quad + \frac{\left|\hat{h}_{n/2}\right|}{n}\left(-1\right)^{m+l} + \sum_{k'=1}^{n/2-1} \frac{2}{n}\sin\left(2\pi(n-k')m/n\right)\sin\left(2\pi(n-k')l/n\right)\left|\hat{h}_{n-k'}\right| \\ &= \frac{\left|\hat{h}_0\right|}{n} + \sum_{k=1}^{n/2-1} \frac{2}{n}\cos\left(2\pi km/n\right)\cos\left(2\pi kl/n\right)\left|\hat{h}_k\right| \\ &\quad + \frac{\left|\hat{h}_{n/2}\right|}{n}\left(-1\right)^{m+l} + \sum_{k'=1}^{n/2-1} \frac{2}{n}\sin\left(2\pi k'm/n\right)\sin\left(2\pi k'l/n\right)\left|\hat{h}^*_{k'}\right| \\ &= \frac{\left|\hat{h}_0\right|}{n} + \sum_{k=1}^{n/2-1} \frac{2}{n}\cos\left(2\pi km/n\right)\cos\left(2\pi kl/n\right)\left|\hat{h}_k\right| \\ &\quad + \frac{\left|\hat{h}_{n/2}\right|}{n}\left(-1\right)^{m+l} + \sum_{k=1}^{n/2-1} \frac{2}{n}\sin\left(2\pi km/n\right)\sin\left(2\pi kl/n\right)\left|\hat{h}_k\right| \end{aligned} \tag{A6}$$

The first equality follows from the periodicity of sin and cos and the conjugate symmetry of the discrete Fourier transform of $\vec{h}$. It is then useful to note that:

$$\begin{aligned} \cos\left(2\pi kl\right) &= \cos\left(2\pi km + 2\pi k(l-m)\right) \\ &= \cos\left(2\pi km\right)\cos\left(2\pi k(l-m)\right) - \sin\left(2\pi km\right)\sin\left(2\pi k(l-m)\right), \text{ and} \\ \sin\left(2\pi kl\right) &= \sin\left(2\pi km + 2\pi k(l-m)\right) \\ &= \sin\left(2\pi km\right)\cos\left(2\pi k(l-m)\right) + \cos\left(2\pi km\right)\sin\left(2\pi k(l-m)\right). \end{aligned} \tag{A7}$$

Plugging these results into the two summations in the last line of Equation A6 we find:

$$\begin{aligned} Q_{ml} &= \frac{\left|\hat{h}_0\right|}{n} + \frac{\left|\hat{h}_{n/2}\right|}{n}\left(-1\right)^{m+l} + \frac{2}{n}\sum_{k=1}^{n/2-1}\left|\hat{h}_k\right|\cos\left(2\pi k(l-m)/n\right) \\ &= \frac{\left|\hat{h}_0\right|}{n} + \frac{2}{n}\sum_{k=1}^{n/2-1}\left|\hat{h}_k\right|\cos\left(2\pi k(l-m)/n\right), \end{aligned} \tag{A8}$$

where in the very last step we have used the fact that for a band-limited function $\hat{h}_{n/2} = 0$. Now consider the sum appearing in the denominator of the diagonal elements of $\mathbf{Q}_S$:

$$Q^{-1}_{S,ii} = \sum_{j=0}^{n-1} Q_{ij} = \left|\hat{h}_0\right| + \frac{2}{n}\sum_{k=1}^{n/2-1}\left|\hat{h}_k\right|\sum_{j=0}^{n-1}\cos\left(2\pi k(i-j)/n\right). \tag{A9}$$

The inner summation of the second term always yields zero. Therefore, using the fact that $\vec{h}$ is a normalized PSF:

$$Q^{-1}_{S,ii} = \left|\hat{h}_0\right| = 1 \tag{A10}$$

So $\mathbf{Q}_S$ is just the identity matrix.

Then it remains to calculate $\mathbf{V} \cdot \mathbf{U}^T$:

$$\sum_{k=0}^{n-1} V_{mk}U_{lk} = \frac{z_0}{n} + \frac{2}{n}\sum_{k=1}^{n/2-1} \cos\left(2\pi km/n\right)\cos\left(2\pi kl/n + \theta_k\right) + \frac{z_0 z_{n/2}}{n}\left(-1\right)^{m+l} + \frac{2}{n}\sum_{k=n/2+1}^{n-1} \sin\left(2\pi km/n\right)\sin\left(2\pi kl/n + \theta_k\right) \tag{A11}$$

The same sequence of transformations used in Equations A5–A8, plus the properties in this case of z_0 and $z_{n/2}$, leads to:

$$\begin{aligned}\sum_{k=0}^{n-1} V_{mk}U_{lk} &= \frac{z_0}{n} + \frac{z_0 z_{n/2}}{n}\left(-1\right)^{m+l} + \frac{2}{n}\sum_{k=1}^{n/2-1} \cos\left(2\pi k(l-m)/n + \theta_k\right) \\ &= \frac{1}{n} + \frac{2}{n}\sum_{k=1}^{n/2-1} \cos\left(2\pi k(l-m)/n + \theta_k\right)\end{aligned} \tag{A12}$$

In the case that $\vec{h}$ expresses a shift of size Δ, the complex phase of $\hat{h}_k$ can be expressed in terms of that shift as:

$$\theta_k = 2\pi\Delta k/n, \tag{A13}$$

which allows us to write:

$$\sum_{k=0}^{n-1} V_{mk}U_{lk} = \frac{1}{n} + \frac{2}{n}\sum_{k=1}^{n/2-1} \cos\left(2\pi k(l-m+\Delta)/n\right) \tag{A14}$$

We can then perform the following manipulation, where we will define $\Delta_{lm} = l - m + \Delta$:

$$\begin{aligned}\sum_{k=0}^{n-1} V_{mk}U_{lk} &= \frac{1}{n} + \frac{2}{n}\sum_{k=1}^{n/2-1} \cos\left(\pi k\Delta_{lm}/(n/2)\right) \\ &= \frac{1}{n} + \frac{1}{2}\sum_{k=1}^{n/4-1} \frac{4}{n}\cos\left(\pi(k-1/2)\Delta_{lm}/(n/4)\right) \\ &\quad + \frac{1}{2}\sum_{k=1}^{n/4-1} \frac{4}{n}\cos\left(\pi k\Delta_{lm}/(n/4)\right),\end{aligned} \tag{A15}$$

which breaks the sum up into two sums. In the limit $n \to \infty$:

$$\lim_{n\to\infty} \frac{1}{n}\sum_{k=1}^{n} \cos\left(\pi(k-1/2)x/n\right) = \mathrm{sinc}(\pi x). \tag{A16}$$

This limit allows us to write:

$$\lim_{n\to\infty} \sum_{k=0}^{n-1} V_{mk}U_{lk} = \frac{1}{2}\mathrm{sinc}(\pi\Delta_{lm}) + \lim_{n\to\infty} \frac{1}{2}\sum_{k=1}^{n/4-1} \frac{4}{n}\cos\left(\pi k\Delta_{lm}/(n/4)\right), \tag{A17}$$

The remaining summation can be manipulated in the same manner as the first one, leading to:

$$\lim_{n\to\infty} \sum_{k=0}^{n-1} V_{mk}U_{lk} = \frac{1}{2}\mathrm{sinc}(\pi\Delta_{lm})\frac{1}{4}\mathrm{sinc}(\pi\Delta_{lm}) + \lim_{n\to\infty} \frac{1}{4}\sum_{k=1}^{n/8-1} \frac{8}{n}\cos\left(\pi k\Delta_{lm}/(n/8)\right). \tag{A18}$$

This recursion then leads to:

$$\lim_{n\to\infty} \sum_{k=0}^{n-1} V_{mk}U_{lk} = \mathrm{sinc}(\pi\Delta_{lm}) \tag{A19}$$

We can derive this result in a slightly different way which will be helpful in the next section. We can rewrite the normal equations:

$$\begin{aligned}\vec{S}_F &= \left(\mathbf{A}^T \cdot \mathbf{N}^{-1} \cdot \mathbf{A}\right)^{-1} \cdot \mathbf{A}^T \cdot \mathbf{N}^{-1} \cdot \vec{f} \\ &= \mathbf{Q}^{-1} \cdot \mathbf{Q}^{-1} \cdot \mathbf{A}^T \cdot \mathbf{N}^{-1} \cdot \vec{f}.\end{aligned} \tag{A20}$$

and then we can write:

$$\vec{S}_G = \mathbf{R} \cdot \mathbf{S}_F = \mathbf{Q}_S \cdot \mathbf{Q}^{-1} \cdot \mathbf{A}^T \cdot \mathbf{N}^{-1} \cdot \vec{f}. \tag{A21}$$

It will be convenient to write $\mathbf{Q}$ differently than above. In this case, we will use the fact that the discrete Fourier transform matrix

$$T_{jk} = \exp\left(-2\pi i\, jk/n\right) \tag{A22}$$

can be used to diagonalize the circulant matrix $\mathbf{A}$:

$$\mathbf{A} = \mathbf{T}^* \cdot \mathbf{H} \cdot \mathbf{T}, \tag{A23}$$

where $H_{jk} = \delta_{jk}\hat{h}_k$. This fact can be used to find the corresponding diagonalization of the inverse covariance matrix:

$$\mathbf{C}^{-1} = \mathbf{A}^T\mathbf{A} = \mathbf{T} \cdot \mathbf{H} \cdot \mathbf{T}^* \cdot \mathbf{T}^* \cdot \mathbf{H} \cdot \mathbf{T} \tag{A24}$$

Using the fact that $\vec{h}$ is real, and thus $\hat{h}_k = \hat{h}^*_{n-k}$, we can rewrite the last three terms as:

$$\mathbf{C}^{-1} = \mathbf{T} \cdot \mathbf{H} \cdot \mathbf{T}^* \cdot \mathbf{T} \cdot \mathbf{H} \cdot \mathbf{T}^*, \tag{A25}$$

leading to:

$$\mathbf{C}^{-1} = \mathbf{T} \cdot \mathbf{H}^2 \cdot \mathbf{T}^*. \tag{A26}$$

The square root can be written as:

$$\mathbf{Q} = \mathbf{T} \cdot |\mathbf{H}| \cdot \mathbf{T}^*. \tag{A27}$$

Then the full solution is:

$$\vec{S}_G = \mathbf{Q}_S \cdot \mathbf{T} \cdot |\mathbf{H}|^{-1} \cdot \mathbf{T}^* \cdot \mathbf{T} \cdot \mathbf{H} \cdot \mathbf{T}^* = \mathbf{Q}_S \cdot \mathbf{T} \cdot \mathbf{\Theta} \cdot \mathbf{T}^* \cdot \mathbf{N}^{-1} \cdot \vec{f}, \tag{A28}$$

where:

$$\Theta_{jk} = \delta_{jk} \exp\left(-2\pi i\, \theta_k/n\right) \tag{A29}$$

and $\hat{h}_k = |\hat{h}_k| \exp(-2\pi\, \theta_k)$. In the case we are considering, we can treat $\vec{h}$ as even around some point, and therefore its complex phase is only due to the shift Δ from that center point:

$$\Theta_{jk} = \delta_{jk} \exp\left(-2\pi i\, \Delta k/n\right). \tag{A30}$$

We need to calculate $\mathbf{Q}_S$:

$$\begin{aligned}Q^{-1}_{S,ll} &= \sum_{j=0}^{n-1} Q_{lj} \\ &= \sum_{j=0}^{n-1}\sum_{k=0}^{n-1} T_{lk} \left|\hat{h}_k\right| T^*_{kj} \\ &= \sum_{k=0}^{n-1} T_{lk} \left|\hat{h}_k\right| \sum_{j=0}^{n-1} T^*_{kj} \\ &= \sum_{k=0}^{n-1} T_{lk} \left|\hat{h}_k\right| \sqrt{n}\delta_{0k} \\ &= \left|\hat{h}_0\right|\end{aligned} \tag{A31}$$

which again just equals unity.

Thus:

$$\vec{S}_G = \mathbf{T} \cdot \mathbf{\Theta} \cdot \mathbf{T}^* \cdot \mathbf{N}^{-1} \cdot \vec{f}. \tag{A32}$$

If we set $\mathbf{N}$ to the identity matrix, this result discrete Fourier transforms the initial vector of data, applies a factor in Fourier space that corresponds to a shift, and Fourier transforms back.

REFERENCES